PAPER

Check for updates

View Article Online
View Journal | View Issue

Bioorthogonal oncolytic-virus nanovesicles combined bio-immunotherapy with CAR-T cells for solid tumors†

Guojun Huang, [ID] ‡[a] Yiran He,‡[a,b] Xiaocong Chen,[a] Ting Yin, [ID] [a] Aiqing Ma,[a] Lizhen Zhu,[a] Liqi Chen,[a,b] Ruijing Liang, [ID] [a,b] Pengfei Zhang, [ID] *[a,b] Hong Pan [ID] *[a,b] and Lintao Cai [ID] *[a,b,c]

Various oncolytic viruses (OVs) have been adopted as therapeutic tools to increase the efficacy of chimeric antigen receptor (CAR)-T cells against solid tumors. However, the therapeutic effect of OVs has been limited by pre-existing neutralizing antibodies and poor targeting delivery for systemic administration. Herein, we propose using bioorthogonal OV nanovesicles to boost the antitumor effects of CAR-T cells in solid tumors by reshaping the tumor microenvironment. Using a cell-membrane nanomimetic technique, we embedded artificial chemical ligands on cancer cell surfaces and then encapsulated lysoviral particles to obtain dual-targeted OV nanovesicles with bioorthogonal targeting and homologous recognition. OVs can be directly encapsulated into cancer cell nanovesicles and exhibit a liposome-like nanostructure, efficient loading, and excellent tumor-targeting capability. Encouragingly, OV nanovesicles efficiently induced tumor-cell apoptosis while sparing normal tissues and cells, thereby inhibiting tumor growth. Administration of viral nanovesicles effectively increased the secretion of anti-tumor cytokines such as IL-2, TNF-α and IFN-γ, and significantly promoted the infiltration and activation of CD8$^+$CAR-T cells in tumors. Our data suggest that bioorthogonal OV nanovesicles hold great potential to overcome the limitations of CAR-T cells as monotherapies against solid tumors and, thus, drive the clinical application of combination therapy.

Introduction

Chimeric antigen receptor T (CAR-T) cells, as a kind of "living drug", have shown significant promise in clinical trials to treat hematologic malignancies, and are becoming the focus of development in the field of medicine.[1,2] However, due to complex physiologic barriers and tumor immunosuppression, cell-based immunotherapies face challenges in terms of efficacy, metastasis, recurrence and safety for the treatment of solid tumors.[3–5] In particular, the immunosuppressive tumor microenvironment is a major obstacle which seriously inhibits

[a]*Guangdong Key Laboratory of Nanomedicine, CAS-HK Joint Lab of Biomaterials, Shenzhen Institute of Advanced Technology (SIAT), Chinese Academy of Sciences (CAS), Shenzhen, 518055, China. E-mail: lt.cai@siat.ac.cn, hong.pan@siat.ac.cn, pf.zhang@siat.ac.cn*
[b]*University of Chinese Academy of Sciences, Beijing, 100049, China*
[c]*Sino-European Center of Biomedicine and Health, Luohu, Shenzhen 518024, China*
†Electronic supplementary information (ESI) available. See DOI: https://doi.org/10.1039/d4bm01305k
‡These authors contributed equally to this work.

the infiltration and survival of immune cells, and eventually leads to the loss of function of tumor-infiltrating CAR-T cells.[6–8] Clinically relevant efficacy of CAR-T cells is unlikely to occur unless both aspects are tackled simultaneously.

Oncolytic viruses (OVs) can selectively infect, replicate and kill tumor cells without harming normal tissue.[9,10] In addition to this direct oncolytic activity, these viruses can also induce an effective immune response to themselves and to infected tumor cells, thereby enhancing the antitumor effects of the body.[11–14] Studies have shown that OVs can increase the antitumor activity of CAR-T cells, but also enhance the antitumor effects of T cells by delivering tumor-associated antigens, and further promote CAR-T cells to overcome the immunosuppressive tumor microenvironment.[15,16] This represents a unique way of reshaping tumor microenvironments with distinct mechanisms of action, which holds great promise for facilitating immunotherapy using CAR-T cells.[17,18] However, an important issue for OV therapy is safe and effective delivery *in vivo*.[19] Systemic intravenous administration is simpler than intratumoral injection, and could target multiple tumors within the body, which has great potential for clinical application,

especially for treatment of metastatic and hematological tumors.[20,21] However, intravenous administration has the disadvantages of interference by circulating blood components, leading to the failure or rapid clearance of OVs. In addition, viral particles are prone to cause systemic spread, leading to severe non-targeted infections.[22,23] So far, considerable efforts have been devoted to developing new OV delivery systems *in vivo*, such as endogenous bioengineering of OVs, exogenous engineering of PEGlation, and hybrid cell carriers.[13,24,25] How to improve the universality, biocompatibility and targeting efficiency of viral carriers is an urgent problem to be solved for OV-targeted delivery in the body.[26,27]

Due to biomimetic and multi-functionalized properties, cell membrane-camouflage nanocarriers have achieved great success in targeted delivery of drugs and tumor therapy, showing attractive potential in the delivery of active biomolecules, proteins and organisms.[28–30] OVs can also be coated in nanoparticles through camouflaging with cellular membranes, which could block virus neutralization and extend vascular circulation *in vivo*.[31,32] However, major challenges remain with regard to the poor targeting delivery of systemically administered OVs in the body.[33,34] Multiple strategies have exploited naturally or tumor cell-derived extracellular vehicles (EVs) for homologous targeted delivery of exogenous therapeutic reagents, including small-molecule anti-inflammatory drugs, siRNAs, and vaccine-like tumor-associated antigens, for presentation in the immune system.[35–37] More importantly, EVs are easily artificially modified for targeted delivery and feature the characteristics of both nanosized and cell-based drug delivery platforms.[38] For instance, artificial bioorthogonal targeting is capable of efficient, specific and stability properties. It has shown great application potential in the targeted delivery of nanomedicines *in vivo*.[39,40] EVs are being bioengineered with highly stable "mimics" of targeting ligands *via* artificial bioorthogonal modification procedures, which could serve as an ideal OV-delivery system to overcome challenges for cancer therapies by systemic administration.[41]

We proposed a combined therapeutic strategy of bioorthogonal OV nanovesicles for boosting the antitumor effects of CAR-T cells in solid tumors by reshaping the tumor microenvironment (Scheme 1). We employed cell membrane nanomimetic techniques to coat OV particles based on artificial chemical modification to embed bioorthogonal targeting ligands on cancer cell membranes. We showed that OVs could be directly encapsulated into cancer cell nanovesicles and exhibit a liposome-like nanostructure, efficient loading, and excellent cancer-targeting specificities. Encouragingly, the OV/M nanovesicles efficiently inhibited tumor-cell proliferation, induced apoptosis while sparing normal tissues and cells, and facilitated the infiltration and activation of CAR-T cells in mouse xenograft models of cancer *via* artificial bioorthogonal targeting and microenvironment reshaping. Results displayed robust and specific CAR-T-cell activation and proliferation upon infection of cancer cells, enhancing the antitumor efficacy of CAR-T cells. These bioorthogonal OV/M nanovesicles could overcome the limitations of CAR-T cells as
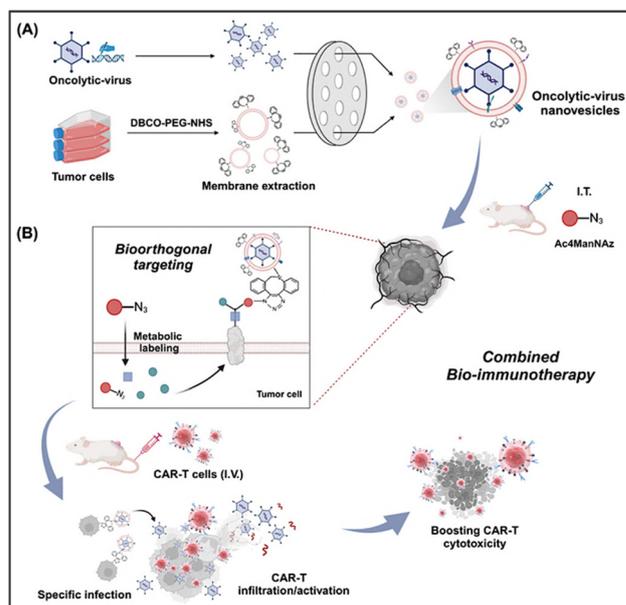
Scheme 1 Design features of oncolytic-virus nanovesicles and combined bio-immunotherapy with CAR-T cells in a tumor-bearing mouse model. (A) Generation of cell membrane nanovesicles from azido-labelled tumor cells. Ovs were encapsulated into cell membrane nanovesicles, thereby forming the bioorthogonal cell-derived membrane nanovesicles-OV complex (OV/M). (B) Dual-targeted OV/M nanovesicles specifically infected azido-labelled tumor tissues by bioorthogonal targeting and homologous recognition. Subsequently, the oncolytic-virus infection significantly reshaped the tumor microenvironment and promoted the infiltration and activation of exogenous T cells, thereby achieving combination bio-immunotherapy with CAR-T cells.

monotherapies in solid tumors and, thus, encourage combination therapy in clinical trials.

Experimental materials and methods

Cells and generation of adenoviruses

Various cell lines were obtained from American Type Culture Collection. SPC-A1 is a human lung adenocarcinoma cell line. SPC-A1-GFP cell is a *GFP* stable-expression SPC-A1 cell line. A549, MCF-7, HEK293T, and MDA-MB231 cells were also used in experiments. These cells were maintained in Dulbecco's modified Eagle's medium (DMEM) supplemented with 10% fetal bovine serum and 5% penicillin and streptomycin. All cell lines were cultured at 37 °C in a humidified atmosphere containing 5% CO_2.

Oncolytic adenovirus H101 is a recombinant type-5 adenovirus with deleted fragments of E1-55 kDa and part of E3 regions. H101 was obtained from Shanghai Sunway Biotech (Shanghai, China). An oncolytic adenovirus is a conditionally replicating adenovirus with a human telomerase promoter and adenoviral E1A gene (hTERTp-E1A). Adenoviruses were expanded in HEK293 host cells and purified and concentrated by the Vivapure® AdenoPACK™ kit (Sartorius). Viral particle (VP) numbers were calculated from optical-density measure-

ments at 260 nm (OD$_{260}$), with one absorbency unit equal to 1×10^{12} VPs mL^{-1}.

Preparation and characterization of bioorthogonal OV/M

Bioorthogonal cell-derived membrane nanovesicles were prepared as shown in the scheme. Briefly, SPC-A1 tumor cells were administered DBCO–PEG$_{2000}$–NHS (20 μM) for 2 h to obtain DBCO-modified tumor cells. Next, the donor tumor cells were harvested and washed thrice with cold PBS. Then, the cells that were resuspended in cold Tris buffer (pH = 7.4) containing 10 mM Tris, 10 mM MgCl$_2$ and 1× EDTA-free protease inhibitor were disrupted overnight at 4 °C. The cell lysate solution was centrifuged at 700g for 10 min at 4 °C. Then, the resulting supernatants were centrifuged at 10 000g for 10 min and centrifuged further at 100 000g for 1 h. The resulting pellet was resuspended with PBS and sonicated for 10 s. Finally, bioorthogonal cell-derived membrane nanovesicles were obtained by ≥15 cycles by extruding the solution through 400 nm polycarbonate membranes. To prepare oncolytic adenovirus-encapsulated nanovesicles (OV/M), the mixture of oncolytic adenovirus particles (1 × 10^{11} VPs mL^{-1}) and OV/M were extruded through 400 nm polycarbonate membranes for 20 cycles, followed by extruding the mixture through 200 nm polycarbonate membranes for ≥5 cycles.

The morphology and internal structure of naked OVs, membrane vesicles, and OV/M were determined by transmission electron microscopy (TEM). The average size and zeta potential of naked OVs, and OV/M were measured using dynamic light scattering (DLS). The encapsulation efficiency of OVs was determined using RT-qPCR.

Western blotting

Western blotting was performed to identify the protein moiety of donor cells, cell membrane-derived nanovesicles, and the oncolytic adenovirus according to standard procedures. The primary antibodies were anti-galectin-3 antibody, anti-N-cadherin antibody, anti-Na$^+$/K$^+$-ATPase antibody and anti-Myc tag antibody. The secondary antibodies were anti-rabbit IgG, anti-mouse IgG, and anti-goat IgG.

Enzyme-linked immunosorbent assay (ELISA)

Cytokine-release assays were performed by co-culturing CAR-T cells and tumor (SPC-A1) cells at a ratio of 1 : 1 for 24 h with or without OV/M administration, respectively. Cell-culture supernatants were collected and then analyzed for the level of IFN-γ, IL-2, and TNF-α using ELISA according to manufacturer (eBioscience, San Diego, CA, USA) protocols. To measure the level of antitumor cytokines in tumors, harvested tumor tissues were weighed and homogenized, and then passed through a 100 μm cell filter. Next, the expression of IL-2, TNF-α and IFN-γ in tumor-tissue supernatants were analyzed by ELISA following the method described above.

Assessment of anti-tumor effects

To assess the anti-tumor effects of OV/M nanovesicles, the toxicity of naked OVs (1 × 10^8 VPs) and OV/M was analyzed in SPC-A1 tumor cells. Cells were seeded at 5000 cells per well in 96-well plates in 10% FBS containing DMEM. Then, cells were incubated with OV, OV/M, CAR-T, or OV/M + CAR-T at the indicated time points. The viability of host cells was real-time monitored from 0 to 48 h post-administration using xCELLigence RTCA (Agilent Technologies). Finally, the morphological characteristics of host cells were recorded by fluorescence microscopy 48 h post-administration.

During cytotoxicity assays, the immunophenotypes of CAR-T cells were identified 24 h after administration of OVs or OV/M according to the ratio of CD4/CD8. T-cell immunostaining was performed by flow cytometry using anti-CD3, anti-CD4 and anti-CD8 antibodies, respectively.

In vitro bioorthogonal targeting ability of OV/M

We wished to determine the *in vitro* binding ability of OV/M on target cells (HepG2, A549, SPC-A1, HEK293T and MDA-MB231). These cells were seeded in confocal dishes (1 × 10^5 cells per well) and pretreated with Ac$_4$ManNAz (20 μM) for 24 h. Dio-labelled DBCO-OV/M were incubated with azido-modified cells for further analysis of bioorthogonal targeting ability. After 3 h incubation at 37 °C in the absence of FBS, cell-culture dishes were washed thrice with PBS to remove free particles. Nuclei were stained with DAPI for 10 min and then underwent confocal laser scanning microscopy with a confocal laser scanning microscope (LSM780).

Biodistribution and viral infection *in vivo*

Animal studies were conducted under recommendations set by the Institutional Review Board of SIAT (serial number: SIAT-IACUC-190220-YYS-PH-A0595). To verify the targeting and biodistribution of OV/M nanovesicles, 6–8-week-old mice pretreated with Ac$_4$ManNAz were intravenously administered OV/M or DBCO-OV/M, respectively. The *in vivo* fluorescence signals of tumor-bearing mice treated with OV/M nanovesicles were recorded using an *in vivo* imaging system from 12 to 72 h after administration. Next, the viral infection of OV/M was analyzed by histological staining. For tissue immunostaining, tumor tissues were harvested at 72 h post-administration and embedded in OCT, cut into 8 μm sections, and then stained with anti-Adv antibodies. Fluorescence images were recorded using confocal microscopy and then analyzed semi-quantitatively using Image-Pro Plus software.

Tumor xenograft models

Briefly, 6–8-week-old Balb/c nude mice were bred in-house according to the protocols of an approved Institutional Animal Care and Use Committee. To create solid-tumor models, Balb/c nude mice were subcutaneously inoculated with 5 × 10^5 CD19$^+$SPC-A1 cells (day 0). When the tumor reached about 100 mm^2, Ac$_4$ManNAz (40 mg kg^{-1}) or an equal volume of PBS was administered into SPC-A1 tumor-bearing mice by intratumoral injection once a day for 4 days. Next, BALB/c nude mice were treated twice with 1 × 10^{10} VPs intravenous injections of OV/M with or without DBCO chemical-group modification; 1 × 10^7 CAR-T cells (~75% CAR$^+$) were infused intravenously at 2

days post-infection as previously described. PBS-treated animals served as controls.

During the period of treatment, the tumor volume (tumor volume = length × width^2/2) and bodyweight of mice were recorded at the indicated times. Tumor-bearing mice were sacrificed upon losing >15% bodyweight or the development of hind-limb paralysis. Tumor tissues from different experimental mice were collected for imaging and weighing. After digestion of tumor tissues with collagenase/DNAase, the infiltration of CAR-T cells in the tumors was analyzed by flow cytometry with anti-CD3, anti-CD8, or anti-myc-alexa 488 antibodies, respectively. Tumor-tissue homogenates were analyzed for TNF-α, IL-2 and IFN-γ using ELISA. Each tumor tissue was derived from a matched tumor-bearing mouse, and all animal samples were involved in the whole experiment (n = 5). Animal experiments were conducted under the guidance of the Animal Care and Use Committee (Shenzhen Institutes of Advanced Technology, Chinese Academy of Sciences; SIAT-IACUC-210304-YYS-TXF-A1712).

Histological staining

Tumor, heart, liver, spleen, lung and kidney tissues were collected immediately 28 days post-administration and frozen in OCT. These tissues were cut into sections (thickness = 8 μm) for subsequent histological staining. Next, tumor-tissue sections were immunostained with anti-Adv, anti-CD3, anti-CD8, anti-CD11b, anti-NK1.1 or anti-Myc tag antibodies, respectively. Fluorescence images were recorded by confocal microscopy and then semi-quantified using Image-Pro Plus software. To assess the pathological changes induced by infusion of OV/M or CAR-T cells, tissues were also stained with hematoxylin and eosin (H&E) according to manufacturer (MilliporeSigma) protocols.

Biosafety analysis

To further evaluate the *in vivo* toxicity of the administration of OV/M or CAR-T cells, biochemical indicators of liver function (AST, ALT) and kidney function (blood urea nitrogen [UREA] and creatinine [CREA]) in serum were measured according to manufacturer protocols by Wuhan Servicebio Technology.

Statistical analyses

Experimental data are the mean ± standard deviation from at least four independent experiments. Differences among groups were calculated using the Student's *t*-test or one-way ANOVA followed by Tukey's post-test (Prism; GraphPad, La Jolla, CA, USA). Differences were considered significant at *p < 0.05, **p < 0.01, and ***p < 0.001.

Results and discussion

Fabrication and characterization of bioorthogonal OV/M nanovesicles

Cancer cell membrane camouflage in a nano-drug shows great potential for tumor targeting delivery through homologous recognition.[42,43] Herein, we applied a biomimetic synthetic strategy to prepare cancer cell membrane-coated OV/M nanovesicles by following a previously reported procedure.[44,45] As expected, the results of polyacrylamide gel electrophoresis and western blotting showed that both adenovirus proteins and membrane adhesive molecules of galectin-3 and *N*-cadherin were detected in nanovesicles (Fig. 1A and S1†), suggesting the OVs had been coated with the SPC-A1 tumor cell membrane. The coating of M on OVs was also confirmed by transmission electron microscopy (TEM). TEM images showed that the vesicle-virus composites were spherical and composed of adenovirus at the core and nanovesicle as shells (Fig. 1B). The size and surface charge of the OV/M nanovesicles were examined by dynamic light scattering (DLS). The average hydrodynamic diameter of OVs was 78 ± 10 nm, which increased slightly to 91 ± 5 nm for OV/M nanovesicles after surface coating of the membrane (Fig. 1C). Zeta-potential measurements of OVs and OV/M nanovesicles revealed negative surface charges of −8.97 ± 0.82 mV and −12.7 ± 1.0 mV (Fig. 1D). The surface charge of the OV/M nanovesicle was as low as that of the nanovesicle, which also confirmed surface coating. Next, cancer cell mem-
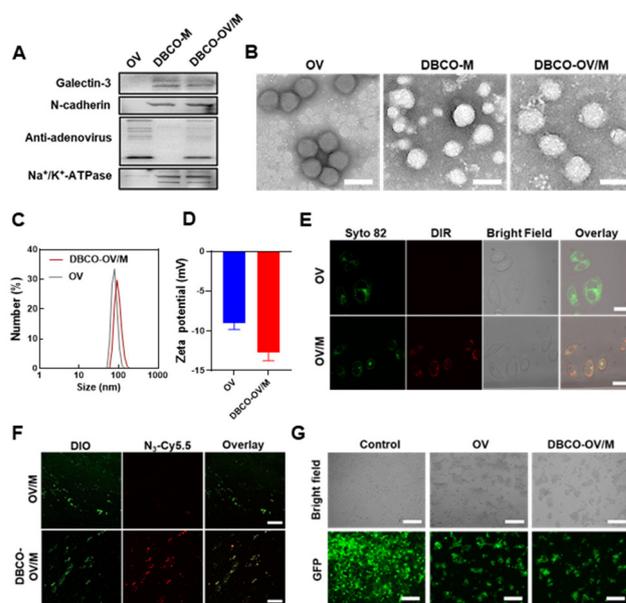
Fig. 1 Fabrication and characterization of bioorthogonal OV/M nanovesicles. (A) Western blotting of adenovirus proteins and membrane-adhesive molecules of galectin-3, *N*-cadherin on OVs, DBCO-/M, and DBCO-OV/M. (B) TEM images of OVs, DBCO-/M, and DBCO-OV/M. TEM images showed that the OV/M vesicle-virus composites were spherical and composed of adenovirus at the core and nanovesicle as shells. Scale bar = 100 nm. (C) Size and (D) surface charge of the nanovesicle-virus composites were examined using dynamic light scattering (DLS). (E) Confocal microscope images of the uptake of OVs, OV/M nanovesicles, and DBCO-OV/M by cells. Viral nuclei stained by syto82 and cell membrane tagged by Dil. Scale bar = 20 μm. (F) Immunofluorescence images of DBCO groups on nanovesicle surfaces detected by the N$_3$-Cy5.5 probe. M was stained by DIO (green). Scale bar = 100 μm. (G) Typical cytopathic effect caused by OVs or DBCO-OV/M in EGFP$^+$SPCA1 cells. Cell morphology and GFP expression were photographed using an inverted microscope 48 h post-infection. Scale bar = 100 μm.

brane-encapsulated OV/M nanovesicles were verified under confocal imaging. Compared with an OV alone, images displayed colocalization of viral nuclei stained by syto82 and cell membrane tagged by Dil in the OV/M nanovesicle-treated group (Fig. 1E), further confirming the cell membrane coating on OV particles. To ascertain whether bioorthogonal chemical groups were labelled on nanovesicles, immunofluorescence imaging was performed with combination of click chemistry labelling using an azide-modified probe. As a result, the azide-modified probe (N_3-Cy5.5) could detect DBCO-labelled nanovesicles on the particle surface, but it was undetectable on unlabelled nanovesicles (Fig. 1F), which indicated that DBCO chemical groups were efficiently modified on nanovesicles.

We wished to determine whether cancer cell membrane coating impaired the virulence of two Ovs. Hence, EGFP-SPCA1 cells were infected with OVs and DBCO-OV/M, and the virus-induced cytopathic effect was monitored under light microscopy. At 48 h after infection, DBCO-OV/M-treated cells had similar growth and GFP expression (Fig. 1G). Besides, the confluence of tumor cells treated by DBCO-OV/M was changed accordingly with that treated by OVs (Fig. S2†). Western blotting confirmed the infecting capability of DBCO-OV/M by detecting adenovirus (Adv) on infected cells (Fig. S3†). These results indicated the unimpaired virulence of DBCO-OV/M, consistent with uncoated OVs.

Bioorthogonal targeting and homologous recognition of OV/M nanovesicles

Considering the targeting properties of bioorthogonal chemistry and homologous recognition, the capability of dual targeting of OV/M nanovesicles was investigated by confocal imaging and flow cytometry. First, HEK293T, MCF-7, A549, and SPC-A1 cells were treated with DIO-stained OV/M nanovesicles and analyzed by flow cytometry. Fig. 2A showed significantly higher uptake efficiency of OV/M nanovesicles by SPC-A1 cells compared with that of other cell lines, indicating the effective homologous targeting of OV/M nanovesicles. Simultaneously, the uptake of OV/M nanovesicles with or without bioorthogonal groups was confirmed using flow cytometry on N_3-SPC-A1 cells (Fig. S4†). As shown in Fig. 2B, tumor cell membrane-coated OV particles significantly increased the cellular uptake compared with that of the OV control, indicating the homologous targeting of OV/M nanovesicles. Notably, the uptake of DBCO-modified OV/M nanovesicles by N_3-SPC-A1 cells was 100%, increased 1.78-fold compared with OV/M, which suggested bioorthogonal targeting further improved the targeting of OV/M nanovesicles to tumor cells. These data clearly demonstrated that OV/M nanovesicles with bioorthogonal targeting and homologous recognition enabled highly efficient targeting and uptake for homologous tumor cells.

To further validate the dual targeting ability of nanovesicles *in vivo*, dynamic imaging was performed to monitor the targeting and enrichment process of nanovesicles on tumor-bearing mice. A SPC-A1 subcutaneous tumor was injected with AC_4ManAz to establish an N_3-SPC-A1 model for bioorthogonal
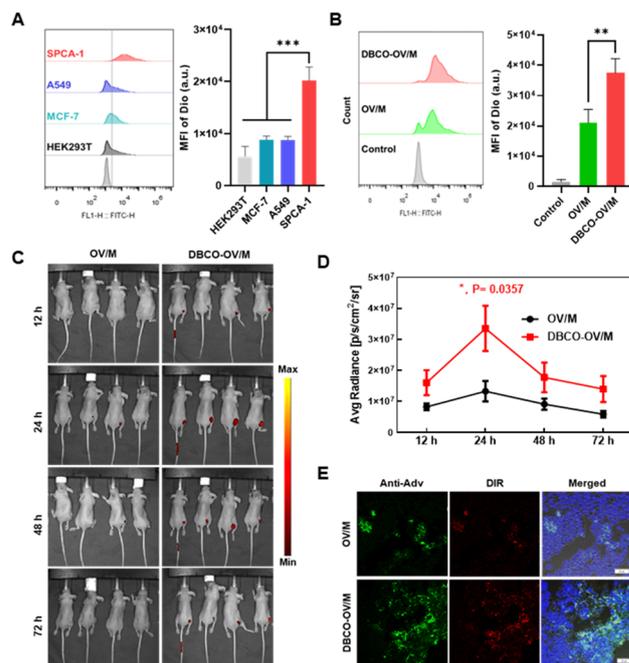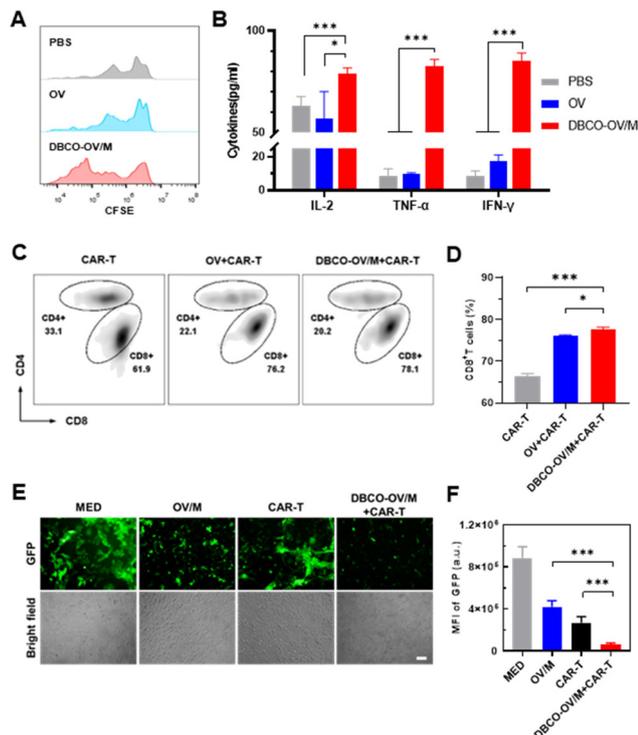

Fig. 2 Bioorthogonal targeting and homologous recognition of OV/M nanovesicles in tumor-bearing mice. (A) Flow cytometry was used to measure the uptake of DIO-stained OV/M nanovesicles by HEK293T, MCF-7, A549, and SPC-A1 cells. (B) Uptake of OV/M nanovesicles or DBCO-OV/M nanovesicles in azido SPC-A1 tumor cells by flow cytometry. (C) *In vivo* fluorescence images and (D) quantification of DBCO-OV/M or OV/M accumulation in tumors at 12–72 h post-injection. DBCO-OV/M and OV/M were stained by DIR. *P < 0.05, unpaired Student's t-test compared with OV/M at 24 h. (E) Immunofluorescence images of excised tumor tissue 72 h after intravenous injection of DBCO-OV/M or OV/M treated by anti-Adv antibodies to visualize viral particles. Scale bar = 20 μm.

targeting analysis (Fig. S5†). *In vivo* imaging showed that DBCO-modified OV/M had stronger tumor-targeting enrichment compared with the OV/M control at 12–72 h post-injection, with a peak especially at 24 h after administration (Fig. 2C and D). After 72 h post-intravenous injection, immunofluorescence analysis of tumor tissue displayed a significant number of viral particles detected by anti-Adv antibodies compared with the control group (Fig. 2E). Simultaneously, the DIR membrane probe showed perfect fluorescence colocalization with viral antibody signals in infected tumor tissues. These results clearly demonstrated that dual targeting of OV/M nanovesicles mediated by bioorthogonal targeting and homologous recognition had superior tumor target delivery capability than single modification *in vivo*.

OV/M nanovesicles enhanced the toxicity of CAR-T cells against tumor cells

Next, we determined whether the bioorthogonal OV/M nanovesicles could enhance the toxicity of CAR-T cells. First, the proliferation of CAR-T cells after treatment with OVs or OV/M was detected by 5,6-carboxyfluorescein diacetate succinimidyl ester (CFSE). As shown in Fig. 3A, DBCO-OV/M-treated CAR-T

Fig. 3 OV/M nanovesicles enhanced the toxicity of CAR-T cells against tumor cells. (A) Proliferation of CAR-T cells after treatment with OV or DBCO-OV/M detected by CFSE. (B) ELISA detected IL-2, TNF-α, and IFN-γ in OVs or DBCO-OV/M synergetic CAR-T cells against CD19+SPC-A1 tumor cells. (C and D) Flow cytometry of the CD4+/CD8+ portion of CAR-T without/with treatment with OVs or DBCO-OV/M. (E) Confocal images and (F) flow cytometry of the toxicity of OV/M + CAR-T cells against tumor cells. Scale bar = 150 μm. ***p < 0.001, one-way ANOVA.

cells exhibited very weak CFSE fluorescence, indicating significant multiplication of CAR-T cells. To detect the secretion of anti-tumor cytokines from OVs or DBCO-OV/M synergetic CAR-T cells, the concentration of IL-2, TNF-α, and IFN-γ was measured by ELISA after coculture with CD19+SPC-A1 tumor cells (Fig. 3B). The cytokine secretion of DBCO-OV/M + CAR-T cells was significantly enhanced compared with that of OV + CAR-T cells, suggesting that the bioorthogonal targeting of DBCO-OV/M nanovesicles could effectively enhance the functions of CAR-T cells. Besides, analysis of the CD4/CD8 portions of OV + CAR-T and DBCO-OV/M + CAR-T cells showed a significant increase in the number of CD8+CAR-T cells compared with that in the CAR-T group (Fig. 3C and D), indicating that OV infection could promote the proliferation of CD8+CAR-T cells. The cytotoxic effect of OV/M nanovesicles, CAR-T cells and OV + CAR-T cells was separately evaluated by GFP-expressing SPC-A1 tumor cells (GFP+SPC-A1). Confocal imaging and flow cytometry showed that OV/M nanovesicles and CAR-T cells had apparent toxicity against tumor cells (Fig. 3E and F). The DBCO-OV/M + CAR-T group had significant toxicity to tumor cells, and the fluorescent intensity of GFP decreased 3-fold compared with CAR-T controls. These findings indicated

that OV/M nanovesicles could deliver OVs to tumor cells and augment the toxic effects of CAR-T cells simultaneously.

CAR-T cells combined with bioorthogonal OV/M nanovesicles for tumor removal

Considering the excellent anti-tumor effect of OV/M nanovesicles in combination with CAR-T cells *in vitro*, we further evaluated the antitumor efficacy of OV/M nanovesicles and CAR-T cells *via* intravenous injection *in vivo* (Fig. 4). The SPC-A1 subcutaneous tumor model on nude mice was utilized to evaluate therapeutic efficacy. PBS (control), OV/M nanovesicles, CAR-T, and OV/M nanovesicles + CAR-T were systemically administered intravenously after the tumor volume reached 80–100 mm³. Mice treated with OV/M nanovesicles exhibited slight inhibition of tumor growth, which was similar to that with CAR-T cells, suggesting that OV/M nanovesicles as virus-delivery nanovesicles showed efficacy against tumor growth (Fig. 4A and B). Also, mice treated with OV/M nanovesicles + CAR-T showed significant antitumor-growth efficacy compared with the PBS group (Fig. 4C and D), whereas mice treated with CAR-T cells exhibited slight antitumor-growth efficacy. Notably, we also utilized the SPC-A1 tumor model for long-term survival analyses. As expected, the OV/M nanovesicles + CAR-T group showed prolonged survival of mice compared with only OV/M nanovesicles or the CAR-T treated group (Fig. 4E).

Bioorthogonal OV/M nanovesicles promote infiltration of CAR-T cells and anti-tumor immune responses

To analysed the immune effects of infection by OV/M nanovesicles, we further evaluated infiltration of exogenous CAR-T cells and their antitumor response. The efficacy of CAR-T cells was directly proportional to the filtration and persistence of CAR-T cells in tumor tissues. We further analysed the accumulation and infiltration of extraneous T cells in tumors using quantitative flow cytometry and immunofluorescence assay at experiment termination. The number of infiltrated CD3+CD8+
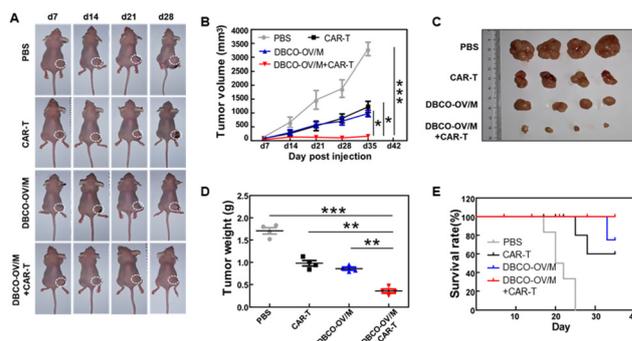

Fig. 4 CAR-T cells combined with bioorthogonal OV/M nanovesicles for tumor removal. (A) Images and (B) tumor volume of mice intravenously treated with PBS (control), DBCO-OV/M nanovesicles, CAR-T, or DBCO-OV/M nanovesicles + CAR-T. (C) Excised tumor and (D) tumor weight from treated mice. (E) Survival of tumor-bearing mice after different treatments.

CAR-T cells in tumor tissue of CAR-T cell-administered mice was about 4.38-fold higher than that in the CAR-T cell control (Fig. 5A and B). These data indicated that there were more exogenous CAR-T cells trafficking into the tumor during treatment. Furthermore, OV/M + CAR-T treatment showed increased production of IL-2, TNF-α and IFN-γ in tumors (Fig. 5C). These results showed that the OV/M + CAR-T group increased the expression of antitumor cytokines compared with the CAR-T group in tumors. Simultaneously, tissue immunofluorescence showed the extraneous infiltrated CD8$^+$ T cells in tumor were about 2.5-fold in CAR-T cell-infused mice treated with OV/M nanovesicles compared with that in the unlabelled CAR-T cell group (Fig. 5D and E), which was consistent with flow-cytometry data. Significant ($p < 0.05$) enhancement of the recruitment and penetration of endogenous monocytes/NK cells was also observed in mice injected with DBCO-OV/M + CAR-T (Fig. 5D), demonstrating activation of the innate immune system against the tumor. The number of infiltrating monocytes or NK cells of the OV/M + CAR-T group was about 6.5-fold or 5-fold higher compared with the CAR-T control (Fig. 5E). Ki67 staining (Fig. 5F) indicated that these tumor slices collected from mice treated by DNP-CAR-T exhibited significantly less tumor-cell proliferation when compared with mice in other groups (Fig. 5G). These data suggested that bioorthogonal OV-nanovesicles dramatically boosted the homing and accumulation of extraneous CAR-T cells, particularly the trafficking and infiltration of cytotoxic CD8$^+$CAR-T cells in deep tumor tissue, which is crucial for elimination of solid tumors.

In vivo toxicity is a critical concern for nanomedicines used in biomedical applications. The similar bodyweight of mice from all groups macroscopically indicated the biosafety of all therapeutics (Fig. S6†). We collected blood and organ samples for blood examination and histology. We measured the concentrations of aspartate aminotransferase (AST) and alanine aminotransferase (ALT) to determine liver function. We measured the concentrations of UREA and CREA to determine kidney function (Fig. S7†). Tissue slices of tumor were also analyzed (Fig. S8†). There were no obvious differences in these parameters in various groups compared with those in the PBS group, demonstrating the favourable *in vivo* compatibility of OV/M + CAR-T.
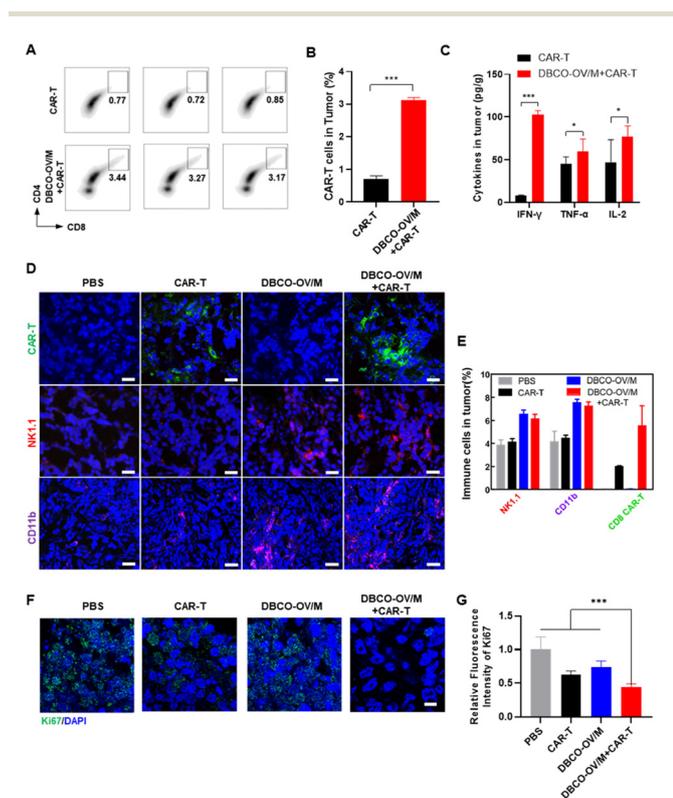
Conclusions

We proposed using bioorthogonal OV to boost the antitumor effects of CAR-T cells in solid tumors by reshaping the tumor microenvironment. Artificial chemical ligands on the cancer cell surface endowed OV particles with capacities of bioorthogonal targeting and homologous recognition. Engineered OV nanovesicles efficiently inhibited tumor growth and induced tumor-cell apoptosis while sparing normal tissues and cells. Combined with cell therapies, administration of bioorthogonal OV/M nanovesicles can significantly promote the infiltration and antitumor activities of CD8$^+$ effector CAR-T cells in tumors with increased secretion of anti-tumor cytokines. These findings shed light on the potential mechanism underlying the enhanced therapeutic efficacy of T cells by dual-targeted OV nanovesicles.

We demonstrated that combination therapy with engineered OVs and adoptively transferred CAR-T cells could amplify antitumor effects. We also shed light on the mechanisms through which OV nanovesicles boost the antitumor efficacy of exogenous CAR-T cells, which might provide valuable insights into its potential clinical applications. Notably, we proposed that combined bio-immunotherapy with OVs and adoptively transferred T cells holds great promise as an effective therapeutic strategy for solid tumors.

Fig. 5 OV/M nanovesicles significantly promoted the infiltration and anti-tumor immune effects of CAR-T cells. (A and B) Infiltrated CAR-T cells within excised CD19$^+$SPC-A1 tumor from CAR-T- and OV/M + CAR-T-treated mice detected by flow cytometry. (C) Intratumoral levels of IFN-γ, TNF-α, IL-2 tested by ELISA. (D) Tissue immunofluorescence of excised tumors from PBS-, DBCO-OV/M-, CAR-T-, and DBCO-OV/M + CAR-T-treated mice. Tumor tissue was stained by anti-NK1.1, anti-CD11b, or anti-CD8 to detect endogenous NK cells, monocytes, and exogenous CAR-T cells, respectively. Scale bar = 50 μm. (E) Quantification of immunofluorescence intensity from tumor-tissue slides. (F) Immunofluorescence images and (G) qualification of Ki67 expression in tumors of PBS-, CAR-T-, DBCO-OV/M-, and DBCO-OV/M + CAR-T-treated mice. Scale bar = 10 μm.

Author contributions

L. Cai, H. Pan, P. Zhang and G. Huang conceived the idea and designed the research. G. Huang and Y. He analyzed the experi-

mental data, performed the preparation of materials and CAR-T cells, and *in vitro* experiments. G. Huang and Y. He performed *in vivo* experiments. G. Huang, X. Chen, T. Yin, and A. Ma performed the data-graphics processing. G. Huang interpreted data and wrote the manuscript. L. Cai, H. Pan, R. Liang and G. Huang contributed to visualization of concepts. L. Cai, and H. Pan contributed to the writing and editing of the manuscript. All authors discussed the results presented in this paper.

Data availability

The data supporting the conclusions reached in our study have been included as part of the ESI.†

Conflicts of interest

There are no conflicts of interest to declare.

Acknowledgements

References

1 D. J. Baker, Z. Arany, J. A. Baur, J. A. Epstein and C. H. June, *Nature*, 2023, **619**(7971), 707–715.

2 M. Elsallab, B. L. Levine, A. S. Wayne and M. Abou-El-Enein, *Lancet Oncol.*, 2020, **21**(2), e104–e116.

3 S. M. Albelda, *Nat. Rev. Clin. Oncol.*, 2024, **21**(1), 47–66.

4 A. J. Hou, L. C. Chen and Y. Y. Chen, *Nat. Rev. Drug Discovery*, 2021, **20**(7), 531–550.

5 J. Crespo, H. Sun, T. H. Welling, Z. Tian and W. Zou, *Curr. Opin. Immunol.*, 2013, **25**(2), 214–221.

6 J. M. Pitt, A. Marabelle, A. Eggermont, J. C. Soria, G. Kroemer and L. Zitvogel, *Ann. Oncol.*, 2016, **27**(8), 1482–1492.

7 J. A. Joyce and D. T. Fearon, *Science*, 2015, **348**(6230), 74–80.

8 J. Zhang, S. Endres and S. Kobold, *Immunotherapy*, 2019, **11**(3), 201–213.

9 H. L. Kaufman, F. J. Kohlhapp and A. Zloza, *Nat. Rev. Drug Discovery*, 2015, **14**(9), 642–662.

10 H. Fukuhara, Y. Ino and T. Todo, *Cancer Sci.*, 2016, **107**(10), 1373–1379.

11 P. K. Bommareddy, M. Shettigar and H. L. Kaufman, *Nat. Rev. Immunol.*, 2018, **18**(8), 498–513.

12 A. Ribas, R. Dummer, I. Puzanov, A. VanderWalde, R. H. I. Andtbacka, O. Michielin, A. J. Olszanski, J. Malvehy, J. Cebon, E. Fernandez, J. M. Kirkwood, T. F. Gajewski, L. Chen, K. S. Gorski, A. A. Anderson, S. J. Diede, M. E. Lassman, J. Gansert, F. S. Hodi and G. V. Long, *Cell*, 2017, **170**(6), 1109–1119.

13 R. Yokoda, B. Nagalo, B. Vernon, R. Oklu, H. Albadawi, T. DeLeon, Y. Zhou, J. Egan, D. Duda and M. Borad, *Oncolytic Virother.*, 2017, **6**, 39–49.

14 A. Samson, K. J. Scott, D. Taggart, E. J. West, E. Wilson, G. J. Nuovo, S. Thomson, R. Corns, R. K. Mathew, M. J. Fuller, T. J. Kottke, J. M. Thompson, E. J. Ilett, J. V. Cockle, P. van Hille, G. Sivakumar, E. S. Polson, S. J. Turnbull, E. S. Appleton, G. Migneco, A. S. Rose, M. C. Coffey, D. A. Beirne, F. J. Collinson, C. Ralph, D. Alan Anthoney, C. J. Twelves, A. J. Furness, S. A. Quezada, H. Wurdak, F. Errington-Mais, H. Pandha, K. J. Harrington, P. J. Selby, R. G. Vile, S. D. Griffin, L. F. Stead, S. C. Short and A. A. Melcher, *Sci. Transl. Med.*, 2018, **10**(422), eaam7577.

15 L. Evgin, T. Kottke, J. Tonne, J. Thompson, A. L. Huff, J. van Vloten, M. Moore, J. Michael, C. Driscoll, J. Pulido, E. Swanson, R. Kennedy, M. Coffey, H. Loghmani, L. Sanchez-Perez, G. Olivier, K. Harrington, H. Pandha, A. Melcher, R. M. Diaz and R. G. Vile, *Sci. Transl. Med.*, 2022, **14**(640), eabn2231.

16 G. Wang, Z. Zhang, K. Zhong, Z. Wang, N. Yang, X. Tang, H. Li, Q. Lu, Z. Wu, B. Yuan, M. Zheng, P. Cheng, A. Tong and L. Zhou, *Mol. Ther.*, 2023, **31**(1), 134–153.

17 S. J. Russell and G. N. Barber, *Cancer Cell*, 2018, **33**(4), 599–605.

18 A. Wing, C. A. Fajardo, A. D. Posey, C. Shaw, T. Da, R. M. Young, R. Alemany, C. H. June and S. Guedan, *Cancer Immunol. Res.*, 2018, **6**(5), 605–616.

19 S. Z. Shalhout, D. M. Miller, K. S. Emerick and H. L. Kaufman, *Nat. Rev. Clin Oncol.*, 2023, **20**(3), 160–177.

20 O. Hemminki, J. M. dos Santos and A. Hemminki, *J. Hematol. Oncol.*, 2020, **13**(1), 84.

21 R. Xie, X. Bi, B. Shang, A. Zhou, H. Shi and J. Shou, *Virol. J.*, 2021, **18**(1), 158.

22 J. Martinez-Quintanilla, I. Seah, M. Chua and K. Shah, *J. Clin. Invest.*, 2019, **129**(4), 1407–1418.

23 C. A. P. Hill, L. Bau and R. Carlisle, *Methods Mol. Biol.*, 2020, **2058**, 7–29.

24 L. Chen, Z. Ma, C. Xu, Y. Xie, D. Ouyang, S. Song, X. Zhao and F. Liu, *Cancer Biol. Med.*, 2023, **20**(11), 830–855.

25 M. Muthana, S. Rodrigues, Y.-Y. Chen, A. Welford, R. Hughes, S. Tazzyman, M. Essand, F. Morrow and C. E. Lewis, *Cancer Res.*, 2013, **73**(2), 490–495.

26 D. Lin, Y. Shen and T. Liang, *Signal Transduction Targeted Ther.*, 2023, **8**(1), 156.

27 M. Kumar, U. Kumar and A. Kumar Singh, *Nano Biomed. Eng.*, 2022, **14**(1), 38–52.

28 R. H. Fang, W. Gao and L. Zhang, *Nat. Rev. Clin Oncol.*, 2023, **20**(1), 33–48.

29 S. Wang, L. Yang, W. He, M. Zheng and Y. Zou, *Small Methods*, 2024, e2400096.

30 W. Fan, B. Yung, P. Huang and X. Chen, *Chem. Rev.*, 2017, **117**(22), 13566–13638.

31 A. T. Power, J. Wang, T. J. Falls, J. M. Paterson, K. A. Parato, B. D. Lichty, D. F. Stojdl, P. A. J. Forsyth, H. Atkins and J. C. Bell, *Mol. Ther.*, 2007, **15**(1), 123–130.

32 Y. Chen, X. Chen, W. Bao, G. Liu, W. Wei and Y. Ping, *Nat. Biotechnol.*, 2024, DOI: **10.1038/s41587-023-02118-7**.

33 W. Ban, J. Guan, H. Huang, Z. He, M. Sun, F. Liu and J. Sun, *Nano Res.*, 2022, **15**(5), 4137–4153.

34 J. Jiang, X. Cui, Y. Huang, D. Yan, B. Wang, Z. Yang, M. Chen, J. Wang, Y. Zhang, G. Liu, C. Zhou, S. Cui, J. Ni, F. Yang and D. Cui, *Nano Biomed. Eng.*, 2024, **16**(2), 152–187.

35 S. Sharma, M. K. Masud, Y. V. Kaneti, P. Rewatkar, A. Koradia, M. S. A. Hossain, Y. Yamauchi, A. Popat and C. Salomon, *Small*, 2021, **17**(42), e2102220.

36 J. P. Goncalves, V. J. Deliwala, D. Kolarich, F. Souza-Fonseca-Guimaraes and J. Wolfram, *Trends Immunol.*, 2022, **43**(11), 864–867.

37 X. Gao, S. Li, F. Ding, H. Fan, L. Shi, L. Zhu, J. Li, J. Feng, X. Zhu and C. Zhang, *Angew. Chem., Int. Ed.*, 2019, **58**(26), 8719–8723.

38 X. Zhang, H. Zhang, J. Gu, J. Zhang, H. Shi, H. Qian, D. Wang, W. Xu, J. Pan and H. A. Santos, *Adv. Mater.*, 2021, **33**(14), e2005709.

39 L. Taiariol, C. Chaix, C. Farre and E. Moreau, *Chem. Rev.*, 2022, **122**(1), 340–384.

40 H. Pan, W. Li, Z. Chen, Y. Luo, W. He, M. Wang, X. Tang, H. He, L. Liu, M. Zheng, X. Jiang, T. Yin, R. Liang, Y. Ma and L. Cai, *Bioact. Mater.*, 2021, **6**(4), 951–962.

41 X. Xu, J. Zheng, N. Liang, X. Zhang, S. Shabiti, Z. Wang, S. Yu, Z.-Y. Pan, W. Li and L. Cai, *ACS Nano*, 2024, **18**(13), 9413–9430.

42 Z. Chen, P. Zhao, Z. Luo, M. Zheng, H. Tian, P. Gong, G. Gao, H. Pan, L. Liu, A. Ma, H. Cui, Y. Ma and L. Cai, *ACS Nano*, 2016, **10**(11), 10049–10057.

43 L. Liu, X. Bai, M. V. Martikainen, A. Kårlund, M. Roponen, W. Xu, G. Hu, E. Tasciotti and V. P. Lehto, *Nat. Commun.*, 2021, **12**(1), 5726.

44 Y. Han, H. Pan, W. Li, Z. Chen, A. Ma, T. Yin, R. Liang, F. Chen, Y. Ma, Y. Jin, M. Zheng, B. Li and L. Cai, *Adv. Sci.*, 2019, **6**(15), 1900251.

45 L. Zhang, T. Yin, B. Zhang, C. Yan, C. Lu, L. Liu, Z. Chen, H. Ran, Q. Shi, H. Pan, A. Ma and L. Cai, *Nano Res.*, 2022, **15**(5), 4224–4232.